Supplementary Information for

Ultrafast probes of electron-hole transitions between two atomic layers

Wen et al.

Supplementary Information for

Ultrafast probes of electron-hole transitions between two atomic layers

Xiewen Wen[2†], Hailong Chen[4†], Tianmin Wu[6†], Zhihao Yu[1†], Qirong Yang[1], Jingwen Deng[1], Zhengtang Liu[1], Xin Guo[1], Jianxin Guan[1], Xiang Zhang[2], Yongji Gong[2], Jiangtan Yuan[2], Zhuhua Zhang[2], Chongyue Yi[5], Xuefeng Guo[1], Pulickel M. Ajayan[2], Wei Zhuang[3*], Zhirong Liu[1]*, Jun Lou[2*], Junrong Zheng[1]*

1 College of Chemistry and Molecular Engineering, Beijing National Laboratory for Molecular Sciences, Peking University, Beijing 100871, China

2 Department of Materials Science and NanoEngineering, Rice University, 6100 Main Street, Houston, Texas 77005-1892, United States

3 State Key Laboratory of Structural Chemistry, Fujian Institute of Research on the Structure of Matter, Chinese Academy of Sciences, Fuzhou, Fujian 350002, China

4 Beijing National Laboratory for Condensed Matter Physics, CAS Key Laboratory of Soft Matter Physics, Institute of Physics, Chinese Academy of Sciences, Beijing 100190, China

5 Department of Chemistry, Rice University, 6100 Main Street, Houston, Texas 77005-1892, United States

6 Department of Chemical Physics, University of Science and Technology of China, Hefei, Anhui 230026, China

†These authors contributed equally to the work

*To whom correspondence should be addressed: junrong@pku.edu.cn, zhengjunrong@gmail.com, jlou@rice.edu, wzhuang@fjirsm.ac.cn,

liuzhirong@pku.edu.cn

Supplementary Figures

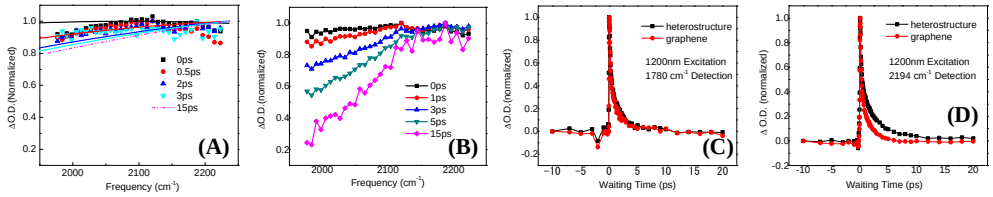

Supplementary Figure 1. *Waiting time dependent IR spectra of monolayer graphene and heterostructure after excitation with 1.03 eV photons. (A) Graphene; (B) heterostructure; (C) pump/probe data detected at 1780 cm^{-1}; (C) pump/probe data detected at 2194 cm^{-1}. Dots are data, and lines are calculations. Calculation parameters: graphene Fermi level* $\mu = -0.19\,eV$, *phonon fraction* $f_{SCOPs} = 0.15$, *photon flux absorbed* $F = 0.0069\,J/m^2$, *pump/probe response time* $t = 170fs$, *and electron-phonon coupling parameter* $\eta = 6.0\,\frac{eV}{\text{Å}}$. *These parameters are used for all calculations for graphene monolayer excited with 1.03 eV.*

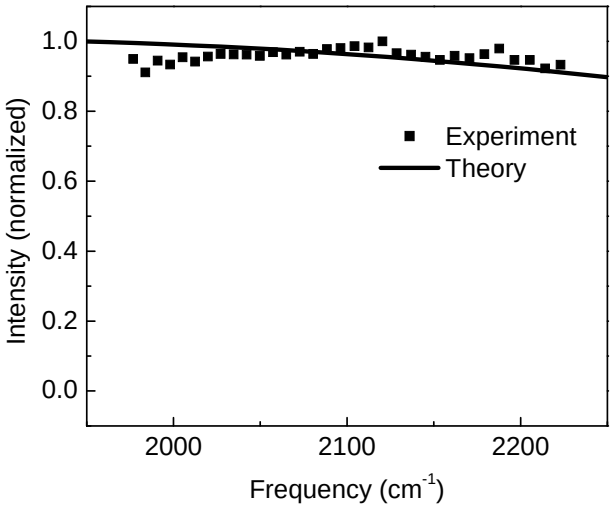

Supplementary Figure 2. *Spectrum of heterostructure at t = 0 ps after excitation*

with 1.03 eV photons. Dots are data, and the line is calculation. Calculation parameters: graphene Fermi level $\mu = -0.17\ eV$*, phonon fraction* $f_{SCOPs} = 0.15$*, photon flux absorbed* $F = 0.0046\ J/m^2$*, response time* $t = 170fs$*, and electron-phonon coupling parameter* $\eta = 6.0\frac{eV}{\text{Å}}$.

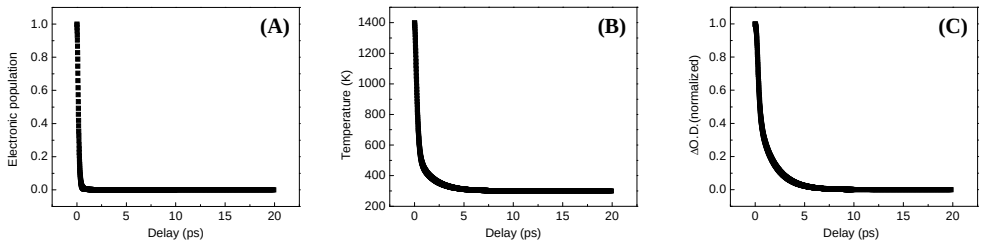

Supplementary Figure 3. *(A) Calculated electronic population relaxation in heterostructure after 1.03 eV excitation. (B) Calculated temperature of graphene in heterostructure. (C) Calculated transient IR signal (2185 cm^{-1}) of graphene in heterostructure after 1.03 eV excitation. Calculation parameters: graphene Fermi level* $\mu = -0.17\ eV$*, phonon fraction* $f_{SCOPs} = 0.15$*, photon flux absorbed* $F = 0.0046\ J/m^2$*, pump response time* $t = 170fs$*, and electron-phonon coupling parameter* $\eta = 6.0\frac{eV}{\text{Å}}$*. Subtracting (C) from the experimental signal of heterostructure (Supplementary Figure 3E) yields the excitonic signal (Supplementary Figure 3F). Here the temperature increase from energy released from exciton formation is ignored. The signal reduction because of exciton formation is not considered either. The effects of these two factors on the graphene signal are opposite. Because of this, we estimate the uncertainty of the exciton formation time introduced by the approximations to be <20% (on average around 25% free carriers form*

excitons). The exciton formation rate is slightly underestimating by this method.

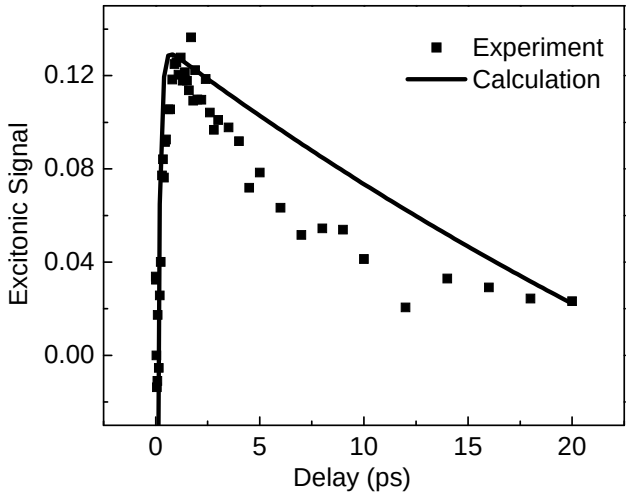

Supplementary Figure 4. *Excitonic signal of heterostructure after 1.03 eV excitation. The data (dots) are obtained by directly subtracting the graphene signal from the heterostructure signal. Calculations (line) show that the excitonic formation time is 325 fs, which is essentially the same as 364 fs of Supplementary Figure 3F. Both time constants are not normalized to the absorption cross section. The line is a bioexponential with t_1=120 fs (electronic decay time constant from graphene calculations) with factor -0.37, and t_2=55 ps with factor 0.37. In Supplementary Figure 3F, the calculation for excitonic signal uses parameters: t_1=120 fs (electronic decay time constant from graphene calculations) with factor -0.33, and t_2=65 ps with factor 0.33.*

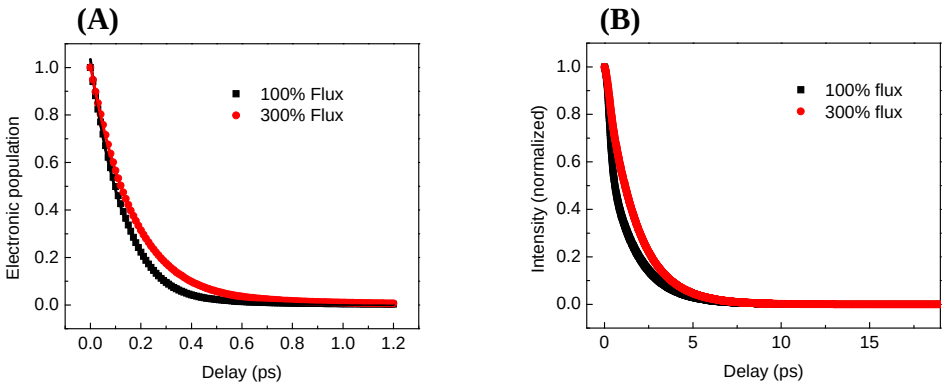

Supplementary Figure 5. *Calculated graphene 400nm-excitation/2185cm^{-1}-detection electronic dynamics (A) and signals (B) with two different excitation fluxes. Calculation parameters: graphene Fermi level* $\mu = -0.17\ eV$, *phonon fraction* $f_{SCOPs} = 0.15$, *photon flux absorbed* $F = 0.0087\frac{J}{m^2}\ (100\%flux)$ *and* $0.0261\frac{J}{m^2}$, *pump response time* $t = 170fs$, *and electron-phonon coupling parameter* $\eta = 6.0\frac{eV}{\text{Å}}$. *The electronic decay time is 130fs with 100% and 170fs with 300% flux.*

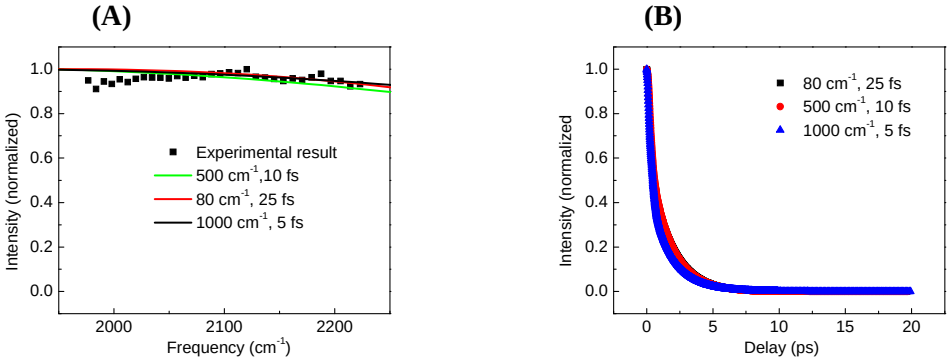

Supplementary Figure 6. *Comparisons of calculations with different electronic dephasing linewidths and times of graphene. Calculation parameters: graphene Fermi level* $\mu = -0.17\ eV$, *phonon fraction* $f_{SCOPs} = 0.20$, $f_{SCOPs} = 0.15$, $f_{SCOPs} = 0.1$ *for calculations with* Γ= 80 cm^{-1} and τ_e = 25 fs, Γ= 500 cm^{-1} and τ_e = 10 fs, Γ=

1000 cm^{-1} and τ_e = 5 fs, *respectively; photon flux absorbed* $F = 0.0087 \frac{J}{m^2}$ $(100\% flux)$*, pump response time* $t = 170 fs$*, and electron-phonon coupling parameter* $\eta = 6.0 \frac{eV}{Å}$*. The parameters only slightly affect the linshape and dynamics.*

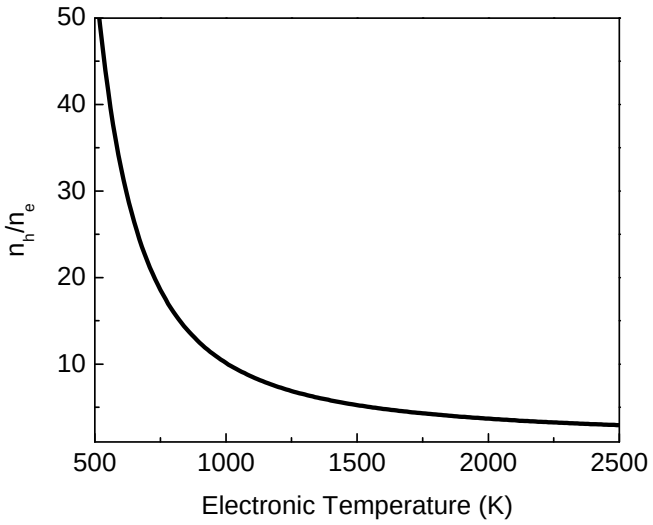

Supplementary Figure 7. *Temperature dependent* n_h/n_e

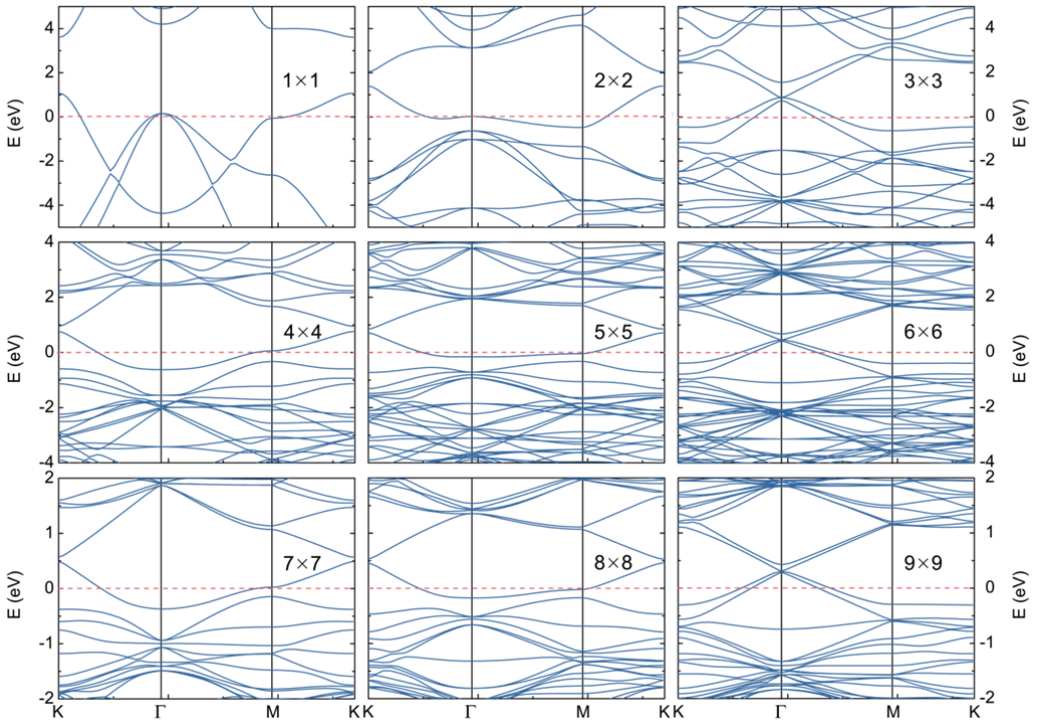

Supplementary Figure 8. *Band structure. Electronic band structures of boron-doped graphene with different primitive cell.*

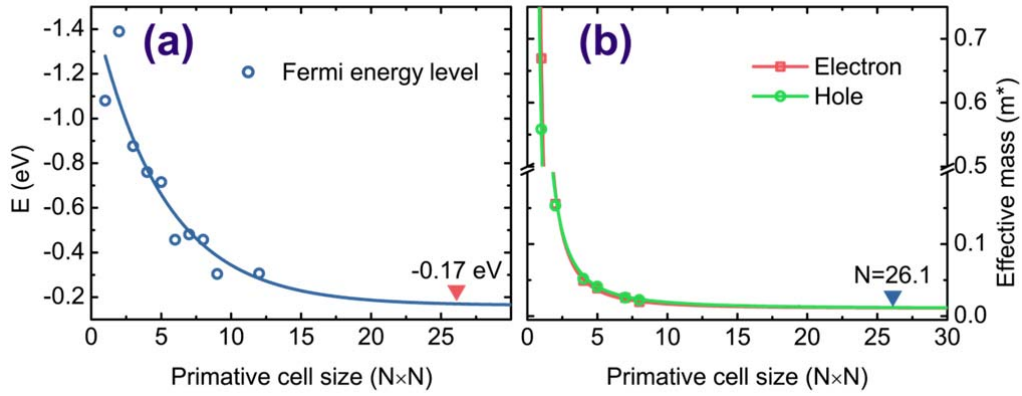

Supplementary Figure 9. ***(a)*** *Fermi energy level of boron-doped graphene with different primitive cell.* ***(b)*** *The effective mass of B-doped system for electron and hole transport with different primitive cell. As the Fermi energy level is -0.17 eV, the primitive cell size is 26.1×26.1, and the corresponding hole and electron effective*

mass is 0.0121 and 0.0116, respectively.

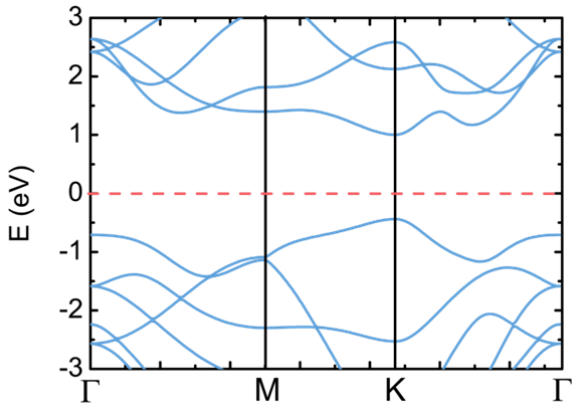

Supplementary Figure 10. *The calculated Electronic band structures of monolayer $MoSe_2$, underestimates the band gap by around 0.5 eV.*

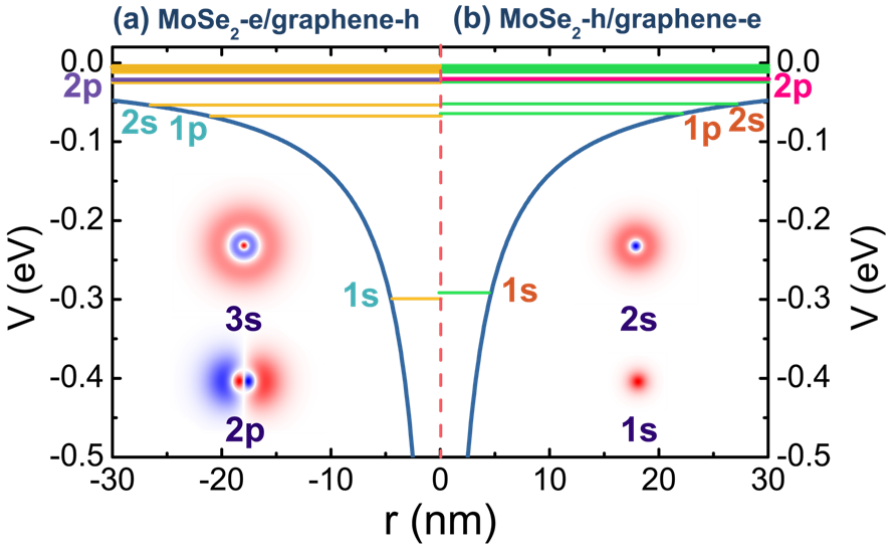

Supplementary Figure 11. *Also Supplementary Figure 3D in main text. A few eigenvalues are shown on the Model Coulomb potential as a function of in-plane radius for an electron-hole pair across the graphene/$MoSe_2$ heterojunction van der Waals interface.* ***(a)*** *Hole is in graphene and electron is in the $MoSe_2$ monolayer.* ***(b)***

Hole is in $MoSe_2$ and electron is in graphene. Wave functions of several states are also shown. (red/blue: positive/negative.)

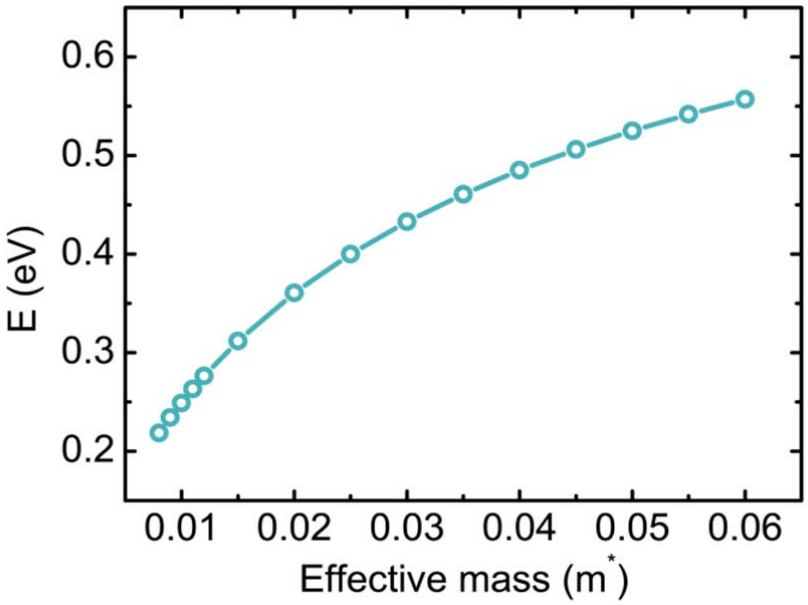

Supplementary Figure 12. *The exciton transition energy (1s-2p) of graphene/$MoSe_2$ correlated with effective mass of the excitonic quasi particle.*

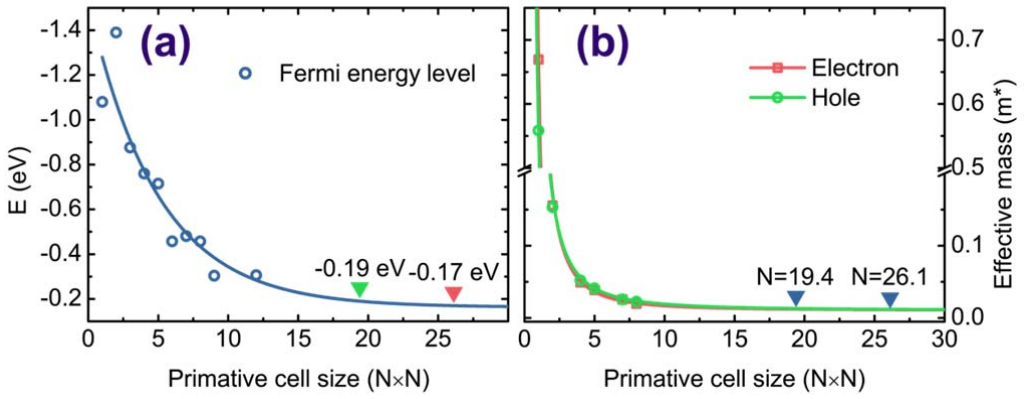

Supplementary Figure 13. ***(a)*** *Fermi energy level of boron-doped graphene with different primitive cell.* ***(b)*** *The effective mass of B-doped system for electron and hole*

transport with different primitive cell. When the Fermi energy level is -0.19 eV, the primitive cell size is 19.4×19.4, and the corresponding hole and electron effective mass is 0.0132 and 0.0122, respectively.

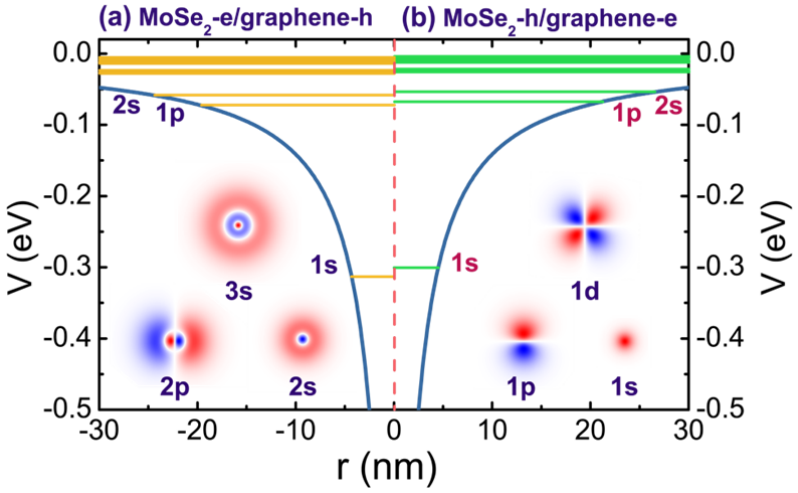

Supplementary Figure 14. *A few eigenvalues are shown on the Model Coulomb potential as a function of in-plane radius for an electron-hole pair across the graphene/$MoSe_2$ heterojunction van der Waals interface.* ***(a)*** *Hole is in graphene and electron is in $MoSe_2$ monolayer.* ***(b)*** *Hole is in $MoSe_2$ slab and electron is in graphene. Several wave functions are also shown. (red/blue: positive/negative.) Fermi level -0.19 eV.*

graphene_hole/$MoSe_2$_electron: $E_{1s\text{-}2p}$= 0.287 eV, $\langle \rho_{CT_{1s}} \rangle = 43.1$ Å

graphene_electron/$MoSe_2$_hole: $E_{1s\text{-}2p}$= 0.276 eV, $\langle \rho_{CT_{1s}} \rangle = 45.1$ Å

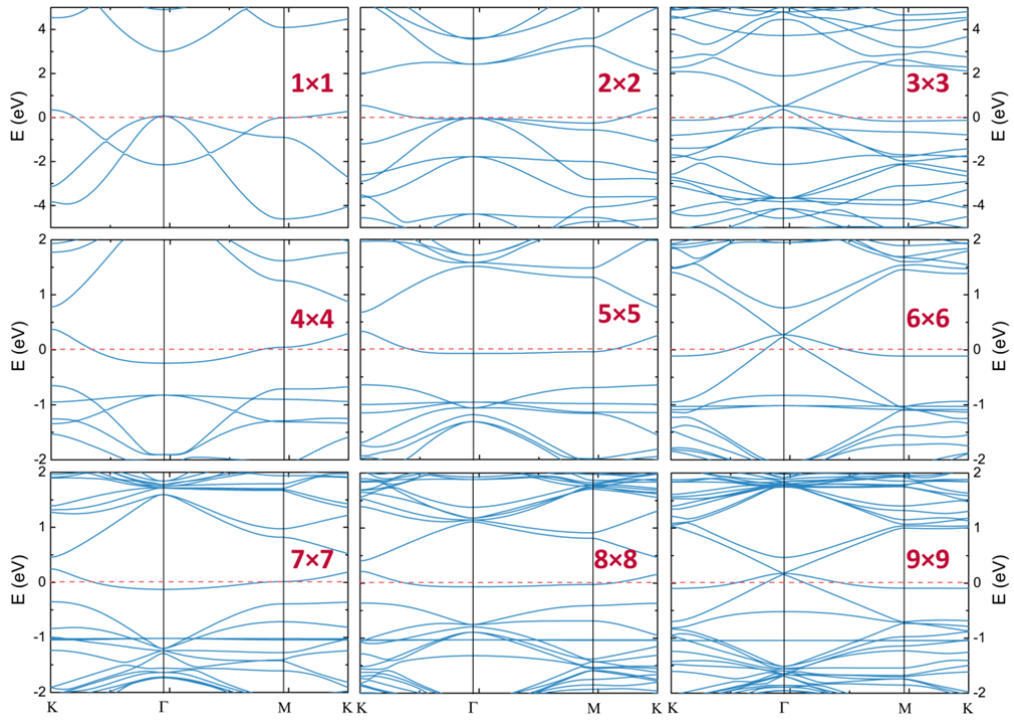

168

169 **Supplementary Figure 15.** *Band structure. Electronic band structures of*

170 *aluminum-doped graphene with different primitive cell.*

171

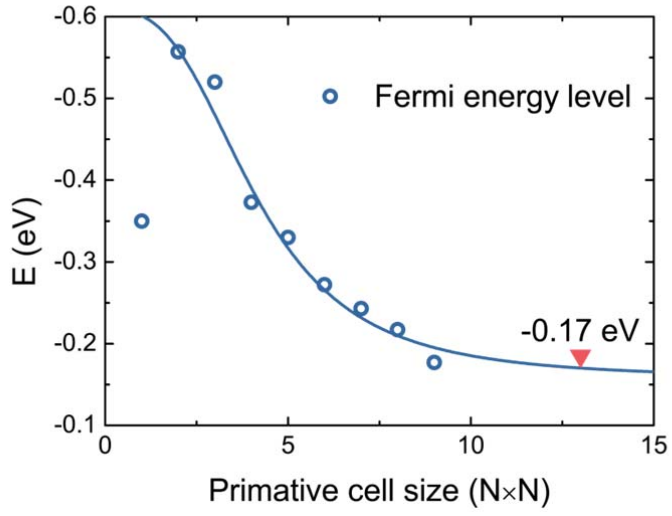

172

173 **Supplementary Figure 16.** *Fermi energy level of aluminum-doped graphene with*

174 *different primitive cell.*

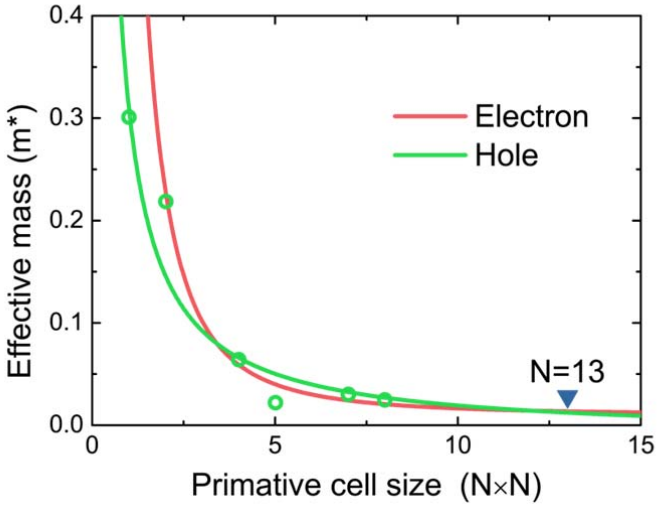

Supplementary Figure 17. *The effective mass of B-doped system for electron and hole transport with different primitive cell. As the Fermi energy level is -0.17 eV, the primitive cell size is 13×13, and the corresponding hole and electron effective mass is 0.0122 and 0.0135, respectively.*

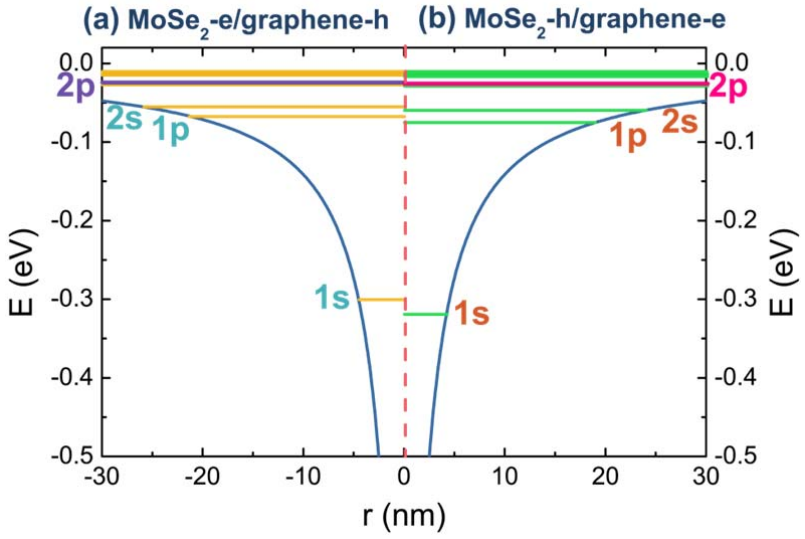

Supplementary Figure 18. *A few eigenvalues are shown on the Model Coulomb*

potential as a function of in-plane radius for an electron-hole pair across the graphene/$MoSe_2$ heterojunction van der Waals interface. ***(a)*** *Hole is in graphene and electron is in the $MoSe_2$ monolayer.* ***(b)*** *Hole is in $MoSe_2$ and electron is in graphene. Wave functions of several states are also shown. (red/blue: positive/negative.)*

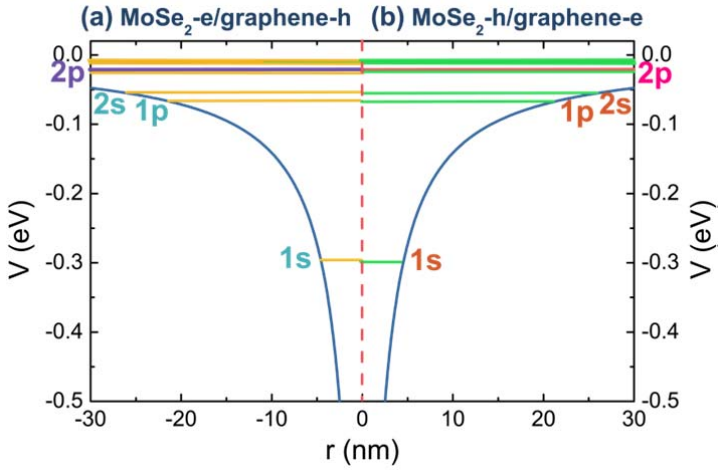

Supplementary Figure 19. *A few eigenvalues are shown on the Model Coulomb potential as a function of in-plane radius for an electron-hole pair across the graphene/$MoSe_2$ heterojunction van der Waals interface.* ***(a)*** *Hole is in graphene and electron is in $MoSe_2$ monolayer.* ***(b)*** *Hole is in $MoSe_2$ slab and electron is in graphene. Several wave functions are also shown. (red/blue: positive/negative.)*

graphene_hole/$MoSe_2$_electron: $E_{1s\text{-}2p}$= 0.273 eV, $\left\langle \rho_{CT_{1S}} \right\rangle = 46.4\text{Å}$

graphene_electron/$MoSe_2$_hole: $E_{1s\text{-}2p}$= 0.274 eV, $\left\langle \rho_{CT_{1S}} \right\rangle = 45.4\text{Å}$

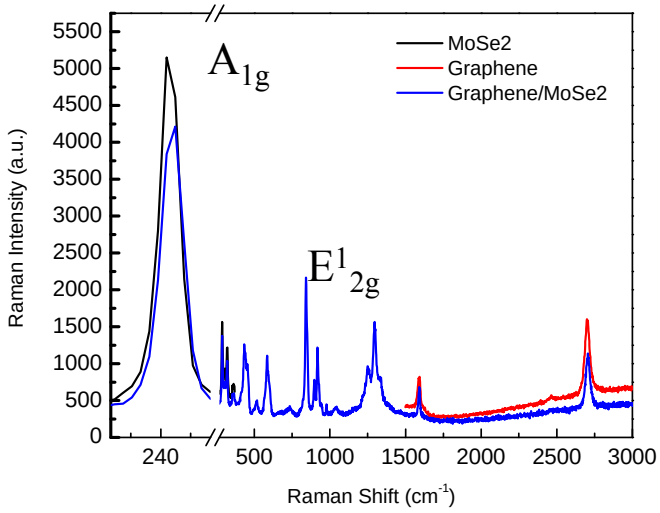

Supplementary Figure 20. *Raman spectroscopy of graphene, $MoSe_2$ and graphene/$MoSe_2$ vdW heterostructure. The frequencies of vibrational modes A_{1g} (242 cm^{-1}) and E_{2g}^1 (288 cm^{-1}) of the standalone $MoSe_2$ sample and the heterostructures match previously reported data of monolayer $MoSe_2$[26]. The characteristic 2D (2690 cm^{-1}) and G (1580 cm^{-1}) peaks of single-layered graphene are present in both the graphene/$MoSe_2$ heterostructures and the standalone graphene sample.*

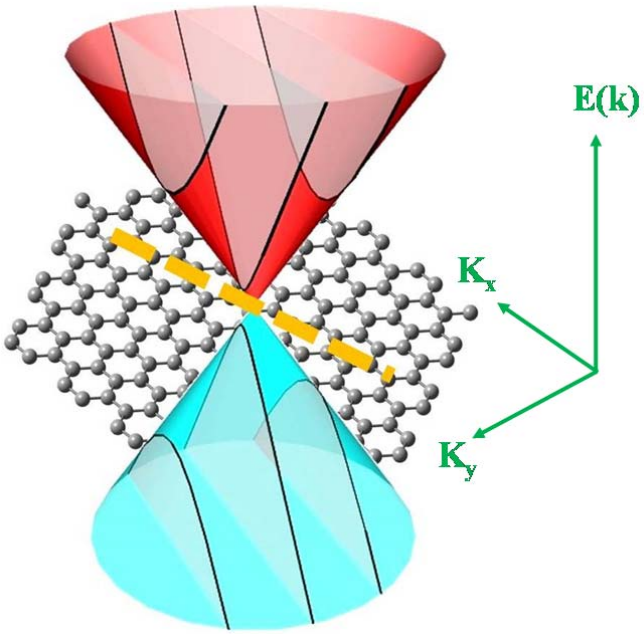

Supplementary Figure 21. *Schematic illustration of the finite effective mass when* ***k*** *deviates away from the Dirac point of graphene. Some k-lines on the Dirac cones along a specified direction were shown as solid lines, which clearly have finite curvature (effective mass).*

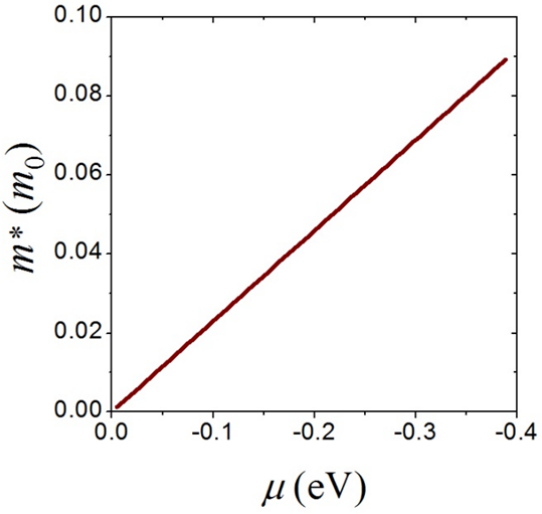

Supplementary Figure 22. *The effective mass m* (in units of m_0, the mass of the free electron) at the level of chemical potential μ along the normal direction of Dirac cone*

in doped graphene. Supplementary Equation (24) is used in the plot.

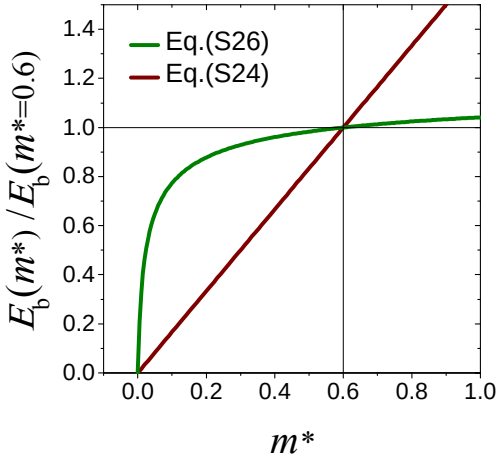

Supplementary Figure 23. *The exciton binding energy as a function of the effective mass m^* (in units of m_0, the mass of the free electron). The binding energy was measured with respective to that of $MoSe_2$ ($m^* = 0.6$). Supplementary Equation (26) and (28) were used in plotting the curves.*

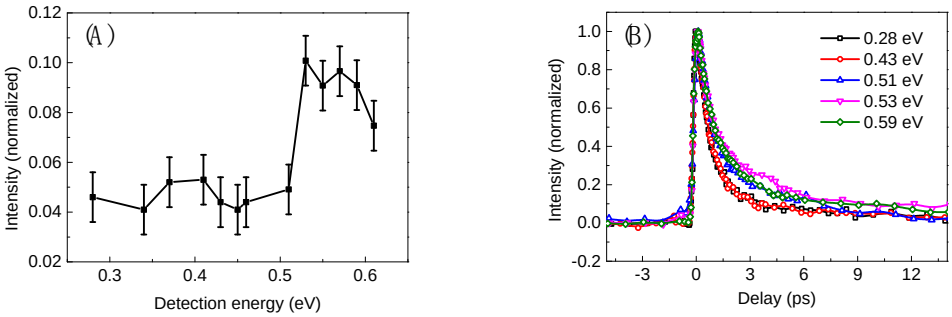

Supplementary Figure 24. *(A) Detection frequency dependent (0.28-0.59 eV) photo responses of monolayer $MoSe_2$ at 10 ps (averaged between 8-12 ps to minimize noise) after excited with 400nm light. A resonance 1s-2p transition peak appears at 0.55 eV. The results indicate that the excitonic binding energy in monolayer $MoSe_2$ is about 0.6 eV. (B) Time dependent dynamics detected at different energy values. The transition between different dynamics starts at 0.51eV. The DFG midIR output from Topas OPA*

combined with HgCdTe detector was used for detection frequencies below 0.47eV. The Idler output of a Palitra OPA combined with an InSb detector was used for detection frequencies above 0.47 eV.

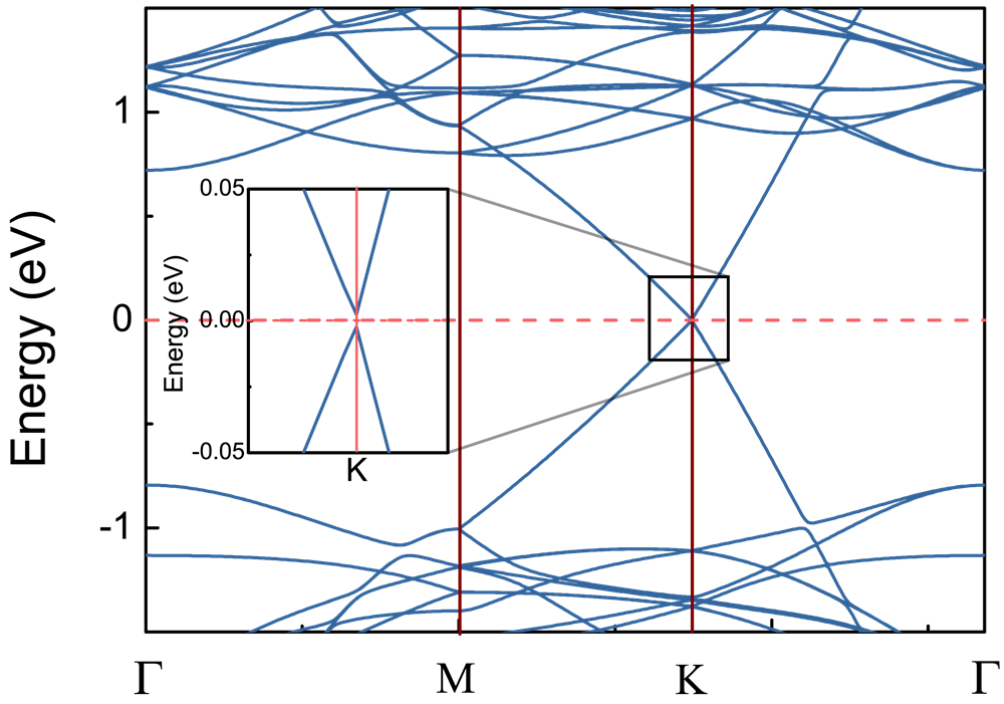

Supplementary Figure 25. *The band structure of a graphene/$MoSe_2$ heterostructure. The symmetry of graphene is broken, and its band structure is opened with a gap of ~ 4.4 meV (the insert). This generates a carrier mass around 0.0004 m_0. This phenomenon was also previously observed in calculations on a graphene/$MoSe_2$ heterostructure (JPCC, 115, 20237, 2011). However, the gap is significantly smaller than the thermal energy (26 meV) at room temperature, the effects it induced at room temperature under which our experiments were conducted are expected to be very small.*

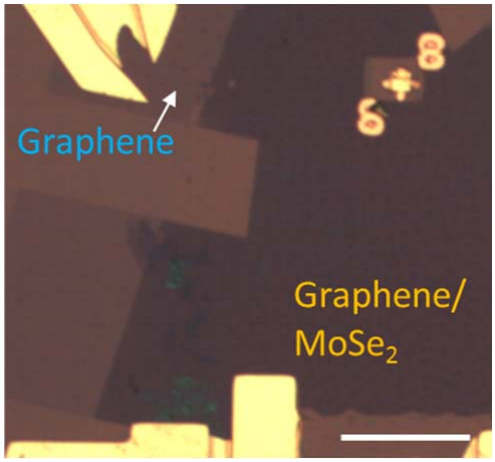

Supplementary Figure 26. *$MoSe_2$/Graphene device used in the measurements, scale bar: 10 μm. $MoSe_2$/graphene vdW heterostructure device for photocurrent measurements. A monolayer of graphene (the lighter image in the center) is transferred on the top of A monolayer of $MoSe_2$ which is on a silicon wafer. Cr/Au (8nm/120nm) electrodes were deposited using E-beam lithography and lift-off technique. Both electrodes are on the top of graphene. One is on the top of graphene underneath which is Si (with a thin layer of SiO_2). The other electrode is on the top of graphene underneath which is $MoSe_2$.*

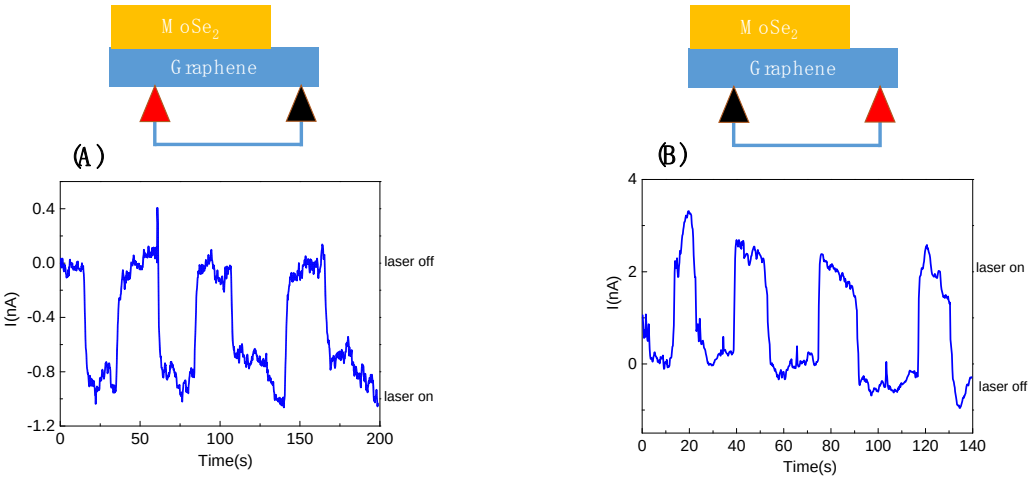

Supplementary Figure 27. *Photocurrent ($I_{ph}=I_{light}-I_{dark}$) of $MoSe_2$/Graphene vdW heterostructure under 980nm excitation. The photons only excite graphene but not $MoSe_2$. Top panel: measurement configurations (A) in which the external current flows from graphene on the top of $MoSe_2$ to graphene on the top of Si (with a thin layer of SiO_2), and (B) the external current direction is flipped. The background current is subtracted. Both results unambiguously demonstrate that the photoexcitation generates an overall electron flow from $MoSe_2$ to graphene inside the heterostructure. After photoexcitation, electrons move from $MoSe_2$ to graphene inside the heterostructure. Therefore, more electrons exist in the area of graphene directly on the top of $MoSe_2$ than in the area of graphene on the top of Si (with a thin layer of*

SiO_2). This results in external current flowing from graphene on the top of Si to graphene on the top of $MoSe_2$. The photocurrent measurements were conducted with a semiconductor parameter analyzer (Agilent 4155C) and a probe station. The source/drain bias V_{sd} =0 and the gate voltage V_g=0 in all tests. The two measurements were conducted under slightly different laser focus sizes.

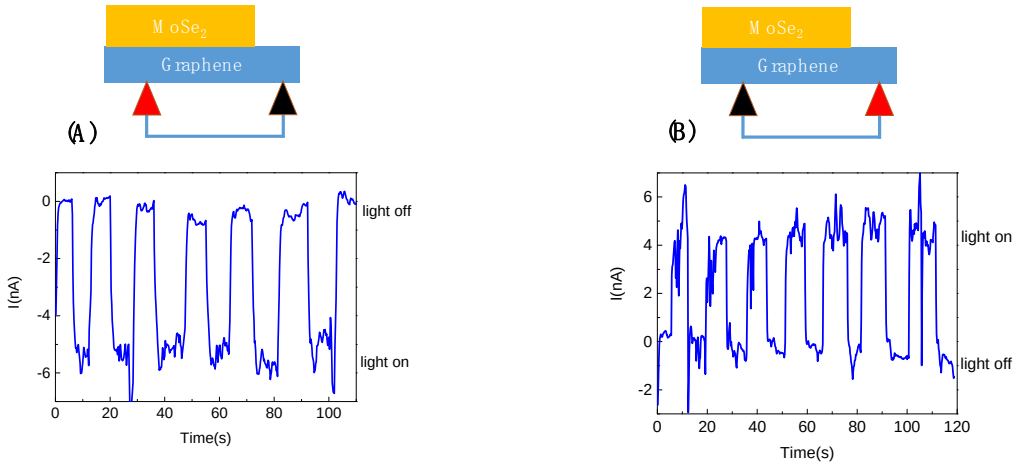

Supplementary Figure 28. *Photocurrent ($I_{ph}=I_{light}-I_{dark}$) of $MoSe_2$/Graphene vdW heterostructure under 405nm excitation. The photons excite both graphene and $MoSe_2$. Top panel: measurement configurations (A) in which the external current flows from graphene on the top of $MoSe_2$ to graphene on the top of Si (with a thin layer of SiO_2), and (B) the external current direction is flipped. The background current is subtracted. Both results unambiguously demonstrate that the photoexcitation generates an overall electron flow from $MoSe_2$ to graphene inside the heterostructure. After photoexcitation, electrons move from $MoSe_2$ to graphene inside the heterostructure. Therefore, more electrons exist in the area of graphene directly on the top of $MoSe_2$ than in the area of graphene on the top of Si (with a thin layer of SiO_2). This results in external current flowing from graphene on the top of Si to graphene on the top of $MoSe_2$.The photocurrent measurements were conducted with a semiconductor parameter analyzer (Agilent 4155C) and a probe station. The source/drain bias V_{sd} =0 and the gate voltage V_g=0 in all tests. Similar photocurrent phenomena was also observed in MoS_2/Graphene vdW heterostructures (ref: Scientific Reports 4, 3826 (2014)).*

Supplementary Notes

Supplementary Note 1: Optical conductivity of graphene

The tight-binding Hamiltonian for the cone-like band structure of graphene is written as

$$H = \begin{bmatrix} 0 & \hbar \upsilon_{\mathrm{F}} \left(k_x + i k_y\right) \\ \hbar \upsilon_{\mathrm{F}} \left(k_x - i k_y\right) & 0 \end{bmatrix}, \tag{1}$$

where υ_{F} is the Fermi velocity, and k_x and k_y are 2D components of the electronic wave vector **k**. With the Hamiltonian, the optical conductivity [$\sigma(\omega)$] is written as the sum of the interband conductivity [$\sigma_{\mathrm{inter}}(\omega)$] and the intraband conductivity [$\sigma_{\mathrm{intra}}(\omega)$] given below[1, 2, 3, 4]:

$$\begin{aligned} &\sigma(\omega) = \sigma_{\mathrm{inter}}(\omega) + \sigma_{\mathrm{intra}}(\omega) \\ &\sigma_{\mathrm{inter}}(\omega) = i\frac{e^2\hbar\omega}{\pi\hbar}\int_0^{+\infty} d\varepsilon \frac{1}{(2\varepsilon)^2 - (\hbar\omega + i\Gamma)^2}\left[f_{\mathrm{FD}}(\varepsilon-\mu) - f_{\mathrm{FD}}(-\varepsilon-\mu)\right], \\ &\sigma_{\mathrm{intra}}(\omega) = i\frac{e^2/\pi\hbar}{\hbar\omega + i\hbar/\tau_e}\int_0^{+\infty} d\varepsilon\left[f_{\mathrm{FD}}(\varepsilon-\mu) + 1 - f_{\mathrm{FD}}(-\varepsilon-\mu)\right] \end{aligned} \tag{2}$$

where f_{FD} is the Fermi-Dirac distribution function, μ is the chemical potential (Fermi energy), and e is the elementary charge. Γ is the broadening of the interband transitions, and τ_e is the relaxation time due to intraband carrier scattering. In literature[5, 6], Γ lies between 0.01 and 0.06 eV while τ_e is in the range of 5 ~ 40 fs. Here, considering that electronic motions typically occur within a few fs rather tens of fs, we use the fast values Γ= 0.062 eV (500 cm^{-1}) and τ_e = 10 fs throughout the study. Nonetheless, effects of these two parameters are also tested and listed in Supplementary Figure 6. It turns out that the results are not very sensitive to the parameter selections.

Applying the Fresnel equations, the change of optical transmission due to the

existence of graphene is given as

$$\frac{\Delta T_s}{T_0} \approx -\frac{2}{\cos\theta + n_{sub}\cos\theta''}\sqrt{\frac{\mu_0}{\varepsilon_0}}\,\mathrm{Re}[\sigma(\omega)] \quad (3)$$

for s-polarized light. θ is the incident angle, and θ'' is the incident angle in the substrate. n_{sub} is the refractive index of the substrate. ε_0 and μ_0 are vacuum permittivity and permeability, respectively. For p-polarized light, the change of optical transmission is

$$\frac{\Delta T_p}{T_0} \approx -\frac{2\cos\theta\cos\theta''}{n_{sub}\cos\theta + \cos\theta''}\sqrt{\frac{\mu_0}{\varepsilon_0}}\,\mathrm{Re}[\sigma(\omega)]. \quad (4)$$

In our experiments, $\theta = 0°$, so we have

$$\frac{\Delta T}{T_0} \approx -\frac{2}{1+n_{sub}}\sqrt{\frac{\mu_0}{\varepsilon_0}}\,\mathrm{Re}[\sigma(\omega)], \quad (5)$$

where n_{sub} = 1.39 for the used substrate (CaF_2).

Supplementary Note 2: Heat transfer between electrons and phonons in graphene

Strongly coupled optical phonons (COPs) are in-plane optical phonons for which intra- and inter-valley carrier scattering can simultaneously conserve energy and momentum[7]. The considered SCOPs include phonons near the Γ-point with energy ~ 200 meV (for intra-valley carrier scattering) and those near the K-point with energy ~150 meV (for inter-valley carrier scattering). The interaction between phonons and electrons/holes in graphene is described by a deformation potential theory,[8, 9] and the transition matrix element is determined to be

329 $$M_{\mathbf{k}',\mathbf{k}}^{(\mathrm{TO\&LO})} \approx 3\eta\sqrt{\frac{\hbar}{4M_C\omega_{\mathrm{phonon}}}}, \tag{6}$$

330 where η is the electron-phonon coupling parameter, and M_C is the mass of a carbon
331 atom. The energy dispersion of the transverse optical (TO) and longitudinal optical
332 (LO) phonon modes is ignored, and Supplementary Equation (6) accounts for the total
333 contribution from TO and LO at Γ- or K-points. Both emission and absorption of the
334 phonons are considered under the second quantization. The probability of scattering
335 from $\mathbf{k}$ to $\mathbf{k}'$ by the SCOPs is

336 $$\begin{aligned} W_{\mathbf{k}',\mathbf{k}}^{(\mathrm{TO\&LO})} &= \frac{2\pi}{\hbar}\left|M_{\mathbf{k}',\mathbf{k}}^{(\mathrm{TO\&LO})}\right|^2\left[N_{\mathbf{q}}\delta\left(\varepsilon_{\mathbf{k}}-\varepsilon_{\mathbf{k}'}+\hbar\omega_{\mathrm{phonon}}\right)+\left(N_{\mathbf{q}}+1\right)\delta\left(\varepsilon_{\mathbf{k}}-\varepsilon_{\mathbf{k}'}-\hbar\omega_{\mathrm{phonon}}\right)\right] \\ &= \frac{9\pi\eta^2}{2M_C\omega_{\mathrm{phonon}}}\left[N_{\mathbf{q}}\delta\left(\varepsilon_{\mathbf{k}}-\varepsilon_{\mathbf{k}'}+\hbar\omega_{\mathrm{phonon}}\right)+\left(N_{\mathbf{q}}+1\right)\delta\left(\varepsilon_{\mathbf{k}}-\varepsilon_{\mathbf{k}'}-\hbar\omega_{\mathrm{phonon}}\right)\right], \end{aligned}$$

337 (7)

338 where $N_{\mathbf{q}}$ is the phonon occupation number described by the Bose-Einstein
339 distribution. The first and second terms in the square brackets correspond to the
340 phonon emission and absorption processes, respectively. Integrating $\mathbf{k}'$ gives the
341 scattering rate of $\mathbf{k}$ as

342 $$\begin{aligned} R_{\mathbf{k}\to *} &= \int W_{\mathbf{k}',\mathbf{k}}^{(\mathrm{TO\&LO})}\frac{A}{(2\pi)^2}d^2\mathbf{k}' \\ &= \frac{9\eta^2}{2\hbar^2\rho v_{\mathrm{F}}^2\omega_{\mathrm{phonon}}}\left[\left(\varepsilon_{\mathbf{k}}+\hbar\omega_{\mathrm{phonon}}\right)N_{\mathbf{q}}+\left(\varepsilon_{\mathbf{k}}-\hbar\omega_{\mathrm{phonon}}\right)\left(N_{\mathbf{q}}+1\right)\right], \end{aligned} \tag{8}$$

343 where ρ is the 2D mass density of graphene. Therefore, the rate of phonon emission
344 per unit area is

345 $$\begin{aligned} \frac{dN_{\mathrm{emission}}}{dt} &= \int\frac{9\eta^2}{2\hbar^2\rho v_{\mathrm{F}}^2\omega_{\mathrm{phonon}}}\left(\varepsilon_{\mathbf{k}}-\hbar\omega_{\mathrm{phonon}}\right)\left(N_{\mathbf{q}}+1\right)f_{\mathrm{FD}}\left(\varepsilon_{\mathbf{k}}\right)\left(1-f_{\mathrm{FD}}\left(\varepsilon_{\mathbf{k}}-\hbar\omega_{\mathrm{phonon}}\right)\right)\frac{1}{(2\pi)^2}d^2\mathbf{k} \\ &= \frac{9\eta^2}{4\pi\left(\hbar v_{\mathrm{F}}\right)^4\rho\omega_{\mathrm{phonon}}}\left(N_{\mathbf{q}}+1\right)\int\varepsilon_{\mathbf{k}}\left(\varepsilon_{\mathbf{k}}-\hbar\omega_{\mathrm{phonon}}\right)f_{\mathrm{FD}}\left(\varepsilon_{\mathbf{k}}\right)\left(1-f_{\mathrm{FD}}\left(\varepsilon_{\mathbf{k}}-\hbar\omega_{\mathrm{phonon}}\right)\right)d\varepsilon_{\mathbf{k}} \end{aligned}$$

(9)

and the rate of phonon absorption is

$$\frac{dN_{\text{adsorption}}}{dt} = \frac{9\eta^2}{4\pi(\hbar\upsilon_{\text{F}})^4\rho\omega_{\text{phonon}}} N_{\mathbf{q}} \int \varepsilon_{\mathbf{k}} \left(\varepsilon_{\mathbf{k}} + \hbar\omega_{\text{phonon}}\right) f_{\text{FD}}(\varepsilon_{\mathbf{k}}) \left(1 - f_{\text{FD}}(\varepsilon_{\mathbf{k}} + \hbar\omega_{\text{phonon}})\right) d\varepsilon_{\mathbf{k}} \,, \quad (10)$$

which are used to simulate the heat transfer between electrons/holes and SCOPs.

The heat capacity of the SCOPs is described by the Einstein model, and the fraction of Brillouin zone filled by the SCOPs, f_{SCOPs}, is assumed to be temperature independent for simplicity[4]. The energy stored in the SCOP subsystem relaxes at a rate of $1/\tau_{\text{ph}}$ to lower energy phonons[4, 10]. The value of f_{SCOPs} and τ_{ph} are determined by fitting the experimental probe signal profiles.

Supplementary Note 3: Fermi level of graphene in heterostructure

Graphene used in our experiments are p-doped with Fermi level -0.19 eV determined by fitting the transient spectra and dynamics in Supplementary Figure 1 and Supplementary Figure 3E. $MoSe_2$ is n-doped. When the two monolayers were placed together to form a heterostructure, some electrons transfer from $MoSe_2$ to graphene[11], raising the graphene Fermi level to -0.17 eV. The Fermi level of graphene in heterostructure is obtained by fitting the transient IR spectrum of heterostructure at time 0 with 1.03 eV excitation (Supplementary Figure 2). The carrier density of graphene is

$$n = \int \frac{1}{(2\pi)^2} f(\varepsilon - \mu) d^2\mathbf{k} = \int \frac{k}{2\pi} f(\varepsilon - \mu) dk = \int_0^{+\infty} \frac{\varepsilon}{2\pi(\hbar\upsilon_{\text{F}})^2} f(\varepsilon - \mu) d\varepsilon \,, \quad (11)$$

When $|\mu| >> k_B T$, Supplementary Equation 11 can be simplified into（degenerate spin and KK'）:

$$n \approx \frac{\mu^2}{\pi(\hbar \upsilon_F)^2}. \quad (12)$$

According to Supplementary Equation 11&12, the Fermi level increase indicates that about $5 \times 10^{11} \frac{e}{cm^2}$ have transferred from $MoSe_2$ to graphene after they form a heterostructure.

Supplementary Note 4: Calculated IR response of graphene with Fermi level -0.17 eV

In the heterostructure excited with 1.03 eV photons, the initial response is only from graphene. Because of fast interlayer charge transfers, some excited carriers move to $MoSe_2$ very rapidly (< 50 fs) and effectively reduce the electronic temperature in the graphene layer. In our calculations, we consider this problem equivalent to the reduction of excitation flux because the charge transfer and electronic thermalization are extremely fast (< 50 fs), much faster than the exciton formation and electron/phonon couplings. Under ideal fast equilibrium, at most 50% of the excitation energy is transferred to $MoSe_2$ by the transferred carriers. However, in our experiments, this is obviously not likely because very few electrons can reach CBM of $MoSe_2$. Therefore, we set the upper limit of flux reduction as 1/3. Calculation results for the exciton formation time with no flux reduction to 1/3 reduction are all within experimental uncertainty.

Supplementary Note 5: Excitonic signal from direct experimental data subtraction

The excitonic signal presented in Supplementary Figure 3F is obtained by considering pump flux and Fermi level changes. Since these two parameters don't change significantly, we also directly subtract the signal of monolayer graphene from that of heterostructure (both presented in Supplementary Figure 3E) to obtain the excitonic signal. Kinetic analyses on the result by this method are plotted in Supplementary Figure 4. The results from this method and that from the more accurate method in Supplementary Figure 3F turn out to be essentially the same.

Supplementary Note 6: Larger flux results in slower graphene signal decay

$MoSe_2$ absorbs 14% and graphene absorbs 4.14% of 3.1 eV photons. Under ideal fast equilibrium, ~9% of excitation photons would be in either layer of the heterostructure. However, because the graphene Fermi level is between $MoSe_2$ VBM and CBM, more carriers are expected to flow into graphene. From photoluminescence, we can see that around 15% of free carriers that are originally excited in $MoSe_2$ remain in $MoSe_2$. Estimated from the results with 1.03 eV photons, about 33% free carriers form interlayer excitons. These two portions together account for 6% of the 18.14% total absorption. Therefore, the excitation flux the graphene layer gains from interlayer charge transfers must not exceed 12.5% (300% of 4.14%) besides direct absorption. The charge transfers results in higher electronic temperature and slower dynamics in graphene.

411

412 **Supplementary Note 7: $MoSe_2$ bandgap**

413 According to STM measurements[12], the bandgap of $MoSe_2$ monolayer samples
414 on different substrates varies. On graphite, it is 1.94 eV, whereas on bilayer graphene
415 it is 2.18 eV. The PL peak central frequency also varies from 1.67 eV to 1.63 eV at
416 77K. The determined binding energy is 0.55 eV, slightly higher than the theoretical
417 value 0.47 eV[13]. The PL central frequency of our sample at room temperature is 1.56
418 eV (on graphene). 1.56 + 0.47 = 2.03 eV. Considering all results from literature and
419 our own experiments, we adopt around 2.0 eV as the bandgap of $MoSe_2$ in the
420 heterostructures measured in our experiments.

421

422 **Supplementary Note 8: Ratio of electron/hole transferred from graphene to**
423 **$MoSe_2$**

424 The population of electrons in graphene that have higher energy than the CBM
425 value of $MoSe_2$ and thus are capable of interlayer transferring is calculated as

426 $$n_e(T;E_{\mathrm{CBM}}) = \int_{E_{\mathrm{CBM}}}^{+\infty} \frac{\varepsilon}{2\pi(\hbar v_{\mathrm{F}})^2} f(\varepsilon-\mu)d\varepsilon \,. \quad (13)$$

427 Similarly, the population of holes being capable of interlayer transferring is

428 $$n_h(T;E_{\mathrm{VBM}}) = \int_{-\infty}^{E_{\mathrm{VBM}}} \frac{\varepsilon}{2\pi(\hbar v_{\mathrm{F}})^2} f(-\varepsilon+\mu)d\varepsilon \,. \quad (14)$$

429 By subtracting the populations before pumping (T_0=300K), the ratio of n_h/n_e
430 determined is plotted in Supplementary Figure 7. With 100% flux of 1200nm
431 excitation, the electronic temperature reaches 1583K. At this temperature, n_h/n_e is 4.9.

With 2/3 flux, the electronic temperature reaches 1399 K and n_h/n_e is 5.8. Because charge transfers result in a lower temperature, the exact n_h/n_e should lie between these two values. Interlayer charge transfers and electronic thermalization in graphene are extremely fast (<50 fs) [4, 14, 15]. Thus, they can be treated as semi-instantaneous, compared to the electron/hole recombination (100~200 fs) in graphene and the formation of interlayer excitons (~500 fs). Therefore, the transfer of photo-excited charge carriers between two layers forms a quasi-equilibrium in which the electron/hole population ratio in $MoSe_2$ is approximately equal to that in graphene. Once the charge carriers form interlayer excitons, the interlayer quasi-equilibrium is perturbed and more carriers are transferred to $MoSe_2$ as the charge carriers in graphene are continuously adjusting their population distributions. This process makes sure that even though the hole population in graphene below the VBM of $MoSe_2$ is only a small portion of the total number photo-generated, the total number of transferred holes is still substantial. The process results in that the majority of interlayer excitons have their holes in the $MoSe_2$ layer and electrons in graphene. The estimated exciton density is about 0.45×10^{12} cm^{-2} and 0.58×10^{12} cm^{-2} under the excitation photon energy 1.03 eV and 3.1 eV, respectively. Another possible mechanism can also lead to that electrons stay in graphene and holes prefer $MoSe_2$. According to literature[11], charged impurities in $MoSe_2$ and graphene can produce an effective electric field that is from graphene to $MoSe_2$. Such an electric field can provide driving force for holes to move to $MoSe_2$ and for electrons to go to graphene.

Supplementary Note 9: Kinetic analysis

To analyze the electron/hole gas transformation dynamics, we create a kinetic model. In the model, interlayer charge transfers and electronic thermalization in graphene are assumed to be semi-instantaneous. Free carriers (y) in graphene decay with a total rate constant k_3. The interlayer exciton (x) formation rate constant is k_1 and the exciton decay rate constant is k_2. The model can be expressed as

$$\begin{array}{l} y \xrightarrow{k_3} \\ y \xrightarrow{k_1} x \xrightarrow{k_2} \end{array} . \qquad (15)$$

The solution of the kinetic model is

$$\begin{aligned} &\frac{dx}{dt} = k_1[y] - k_2[x] \\ &\frac{dy}{dt} = -k_3[y] \\ &x(t) = \frac{k_1}{k_3 - k_2}(1 - e^{-(k_3 - k_2)t})e^{-k_2 t} \end{aligned} , \qquad (16)$$

where k_3 is obtained from the electronic decay of graphene. k_1 and k_2 are obtained from fitting the experimental excitonic signal.

In Supplementary Figure 3F, $1/k_1 = 364\,fs,\ 1/k_2 = 65\,ps,\ 1/k_2 = 120\,fs$.

In Supplementary Figure 4F, $1/k_1 = 379\,fs,\ 1/k_2 = 55\,ps,\ 1/k_2 = 170\,fs$.

The binding energy of $MoSe_2$ intralayer exciton is >0.4 eV, which exceeds the photon energy of our IR probe. In addition, the optical response of free carriers in $MoSe_2$ is only 1/6 of the free carries in graphene. Therefore, in the kinetic model the contribution from free carriers in $MoSe_2$ is ignored. The response ratio 1/6 is calculated based on experimental results: with the same 3.1 eV excitation, 14% photons are absorbed by $MoSe_2$, producing a signal size of -0.006, whereas 4.14%

photons are absorbed by graphene producing a signal size of -0.011. 0.011/0.006*14%/4.14% ~ 6.

Supplementary Note 10: Exciton and free carrier optical responses

The free carrier optical conductivity from the Drude model[16] is

$$\sigma_{free} = \frac{ne^2\tau}{\mu\left(\omega^2\tau^2+1\right)} = \frac{n\hbar e^2\Gamma_D}{\mu\left[(\hbar\omega)^2+\Gamma_D{}^2\right]}, \quad (17)$$

where n is the carrier population, μ is the reduced mass and Γ_D is the scattering (dephasing) line width. The 1s-2p transition optical conductivity[17] is

$$\sigma_{1s-2p} = \frac{n_X\hbar e^2\Gamma_{1s-2p}\cdot(\hbar\omega)^2 f_{1s-2p}}{\mu\left[((\hbar\omega)^2-E_{res}^2)^2+\left(\hbar\omega\Gamma_{1s-2p}\right)^2\right]}, \quad (18)$$

where E_{res} is the resonant energy. The optical conductivity ratio between the 1s-2p transition and free carrier is therefore:

$$\frac{\sigma_{1s\text{-}2p}}{\sigma_{e\text{-}h}} \approx \frac{2n_X f_{1s-2p}}{\Gamma_{1s-2p}} \Big/ \frac{n_{e\text{-}h}\Gamma_D}{(\hbar\omega)^2} \approx \frac{2f_{1s-2p}(\hbar\omega)^2}{\Gamma_D\Gamma_{1s-2p}}, \quad (19)$$

where f_{1s-2p} is the oscillator strength that can be calculated in the following[18]:

$$\begin{aligned} f_{1s-n} &= \frac{2\mu a^2}{\hbar^2}(E_n-E_0)\frac{\left(n+\frac{1}{2}\right)^5 n^{2n-3}}{(n+1)^{2n+5}} \\ &= \frac{2\mu a^2}{\hbar^2}\cdot\frac{e^2\lambda}{8\pi\varepsilon_0\varepsilon_r a}\left[\frac{1}{(1/2)^2}-\frac{1}{(n+1/2)^2}\right]\frac{\left(n+\frac{1}{2}\right)^5 n^{2n-3}}{(n+1)^{2n+5}} \\ &= \frac{\mu e^2\lambda a}{4\pi\varepsilon_0\varepsilon_r\hbar^2}\left[\frac{1}{(1/2)^2}-\frac{1}{(n+1/2)^2}\right]\frac{\left(n+\frac{1}{2}\right)^5 n^{2n-3}}{(n+1)^{2n+5}} \\ &= \frac{\mu e^2\lambda}{4\pi\varepsilon_0\varepsilon_r\hbar^2}\cdot\frac{4\pi\hbar^2\varepsilon_0\varepsilon_r}{e^2\mu\lambda}\left[\frac{1}{(1/2)^2}-\frac{1}{(n+1/2)^2}\right]\frac{\left(n+\frac{1}{2}\right)^5 n^{2n-3}}{(n+1)^{2n+5}} \\ &= \left[\frac{1}{(1/2)^2}-\frac{1}{(n+1/2)^2}\right]\frac{\left(n+\frac{1}{2}\right)^5 n^{2n-3}}{(n+1)^{2n+5}} \end{aligned} \quad . \quad (20)$$

Based on Supplementary Equation 18, $f_{1s-2p}=0.21$, slightly different from the value 0.32 derived from a non-hydrogen model[17]. Γ_{1s-2p} is experimentally determined

to be 280 cm^{-1}. Using the ratio $\Gamma_D / \Gamma_{1s-2p} = 6$ adopted in literature[18], $\frac{\sigma_{1s\text{-}2p}}{\sigma_{e\text{-}h}}$ is calculated to be 3.6. However, $\frac{\sigma_{1s\text{-}2p}}{\sigma_{e\text{-}h}}$ calculated here is for exciton and free carrier in the same material. In our experiments, the interlayer exciton is within two very different materials of which the free carrier response ratio is 1/6 = $MoSe_2$/graphene. It is reasonable to expect that $\sigma_{1s\text{-}2p}$ of the $MoSe_2$/graphene interlayer exciton is 1~3.5 times (it doesn't go to 6 because the 1s-2p transition is a bound-bound transition and graphene cannot affect it in a way like free carriers) of $\sigma_{1s\text{-}2p}$ of $MoSe_2$, giving $\frac{\sigma_{1s\text{-}2p\text{-}interlayer}}{\sigma_{e\text{-}h\text{-}graphene}} = 0.6 \sim 2.1$. Normalized with the ratio, the excitonic formation time constants obtained from fitting the experimental results in Supplementary Figure 3F&4F are 218 fs~764 fs (Supplementary Figure 3F) and 227 fs~796 fs (Supplementary Figure 4F), respectively.

Supplementary Note 11: Exciton 1s-2p transition energy calculations

Methods:

First-principle calculations in this work are conducted using DFT methods implemented in the Vienna *ab initio* simulation package (VASP)[19]. The projector-augmented-wave (PAW) pseudopotentials and the generalized gradient approximation of Perdew, Burke, and Ernzerhof (PBE) for exchange-correlation functional are adopted in our simulations[20]. In order to study the influence of Fermi level on the electronic properties for hole-doped graphene system, we conducted the first-principle investigation on the electronic band structures of graphene sheets

(N×N×1 primitive unit cell) doped by the Boron atoms (which can effectively modulate the position of Fermi level but minimally alter other physical properties of graphene). For Brillouin zone (BZ) integrations, a Monkhorst-Pack k-point mesh scheme with 7×7×1 are adopted[21]. Meanwhile, for graphene and monolayer $MoSe_2$ system, we use a 9×9×1 k-meshes for Brillouin zone sampling in the Monkhorst-Pack scheme. In order to simulate the graphene/$MoSe_2$ 2D heterostructures, we imposes a commensurability condition between them, where a 4×4 supercell of the graphene is used to match a 3×3 supercell of the $MoSe_2$ monolayer. The lateral lattice parameter for the triangular lattice of graphene/$MoSe_2$ nanocomposite is set to be a(graphene/$MoSe_2$) = (4*a(graphene)+3*a($MoSe_2$)) = 9.912 Å, in which a(graphene) = 2.468 Å and a($MoSe_2$)=3.317 Å are optimized for isolated graphene and monolayer $MoSe_2$, respectively. Since there is only a very small lattice mismatch of ~0.4% between the graphene and the $MoSe_2$ monolayers, the approximation used here is reasonable. Boron-doped graphene/$MoSe_2$ nanocomposite in which one random carbon atom is replaced with a boron atom is also used to study the influence of doping on the thickness of graphene/$MoSe_2$ heterojunction (along z direction). Since the heterostructure contains one graphene and one $MoSe_2$ monolayer, van der Waals (vdW) interactions are taken into account by using the semi-empirical DFT-D3 method[22]. For the pristine as well as the boron-doped graphene/$MoSe_2$ heterojunction, a 5×5×1 Monkhorst-Pack k-point mesh is used. A cutoff of 500 eV is used for the plane-wave expansion of the wave function to converge the relevant quantities. The structure relaxations are carried out until all the atomic forces on each

ion are less than 0.01 eV/Å, enforcing a total energy convergence of 1×10^{-7} eV. To avoid spurious interactions with replicas, a vacuum slab larger than 15 Å is added in the z direction for all system.

Results:

As demonstrated in Supplementary Figure 8, the Fermi energy levels are adjusted, by boron doping, to the valence bands and the whole doping system acts as a p-dopant. Supplementary Figure *9(a)* shows the Fermi energy levels of the doped graphene with different N×N primitive cells. With the decrease of dopant concentration, the Fermi energy level gradually decreases to the experimental value. As the Fermi energy level of boron-doped graphene reaches the experimental value (-0.17eV), the primitive cell size is 26.1×26.1, and the calculated effective mass of B-doped system for electron and hole is 0.0116 and 0.0121, respectively. (Supplementary Figure 9(a))

The optimized thickness between the two layers (C atom - Mo atom) of Boron-doped graphene/MoSe2 heterojunction is 5.178Å, which is very close to the value of undoped heterojunction (5.183Å), thereby low concentration of boron doping does not alter the thickness between the two layers significantly. Furthermore, the in-plane dielectric constant of B-doped graphene is almost equal to the value of pristine graphene when the primitive cell size is larger than 8×8. We set the dielectric constant of graphene/MoSe2 heterojunction as $\bar{\varepsilon} = 4.969$, which is the average value of the calculated in-plane dielectric constant $\varepsilon xx = 3.651$ and 6.287 for graphene and monolayer MoSe2, respectively.

To obtain the potential experienced by an electron at (ρ, z) due to the presence of

a hole at (0, z0), we use a field method described by Smythe23 and extended by Sritharan13:

$$V(\rho) = -\frac{e^2}{4\pi\varepsilon_0\bar{\varepsilon}}\left\{\frac{1}{\sqrt{(z-z_0)^2+\rho^2}} + \sum_{n=0}^{\infty}\left(\frac{\beta_N}{\beta_P}\right)^n\left[\frac{\beta_N/\beta_P}{\sqrt{(z-z_0+2c+2nc)^2+\rho^2}} + \frac{\beta_N/\beta_P}{\sqrt{(z_0-z+2c+2nc)^2+\rho^2}} + \frac{(K_2-K_1)/(K_2+K_1)}{\sqrt{(z+z_0-2a+2nc)^2+\rho^2}} + \frac{(K_2-K_3)/(K_2+K_3)}{\sqrt{(2b-z-z_0+2nc)^2+\rho^2}}\right]\right\}, \quad (21)$$

where $\beta_P = (\bar{\varepsilon}+1)^2$ and $\beta_N = (\bar{\varepsilon}-1)^2$, K1=K3=1 since the graphene/MoSe2 heterojunction is approximated as a single dielectric slab sandwiched between vacuum. When the electron and hole are at different layers, they are assumed to be at the center of the graphene and MoSe2 monolayer along the z direction with a fixed distance of 5.183Å which is the thickness of heterojunction. The exciton is then simplified as a two dimensional quasi-particle24.

When the hole is in graphene and the electron is in the MoSe2 layer, the effective mass of exciton can be obtained from $\frac{1}{\mu} = \frac{1}{m_h^*} + \frac{1}{m_e^*}$, where the effective mass of monolayer MoSe2 conduction band $m_e^* = 0.502m_0$ (Supplementary Figure 10) and the effective mass of B-doped graphene valence band $m_h^* = 0.0121m_0$, m_0 is the free electron mass. Based on the finite element method, we then solved the Schrödinger equation on a 2×103 Å circle plane, with the effective mass of the excitonic quasi particle and aforementioned Coulomb potential. The eigenvalues and selected eigenfunctions calculated are presented in Supplementary Figure 11a. The exciton transition energy between 1s and 2p is E1s-2p= 0.274 eV, and the means radius of wave functions for 1s CT is $\langle\rho_{CT_{1s}}\rangle = 45.3$ Å. The 1s-1p transition energy is also larger than 0.20 eV. Both 1s-1p and 1s-2p transition energy values are close to the

experimental value 0.27 eV.

When electron is in graphene and hole is in MoSe2, the hole and electron effective masses should be the effective masses of the monolayer MoSe2 valence band ($0.583\,m_0$) and B-doped graphene conduction band ($0.0116\,m_0$), respectively. The eigenvalues and selected eigenfunctions are presented in Supplementary Figure 11b. The exciton transition energy between 1s and 2p is E1s-2p= 0.267 eV, and the means radius of wave functions for 1s CT is $\langle \rho_{CT_{1s}} \rangle = 46.6$ Å. There is a 0.007eV difference between the binding energies in two conditions. In our experiments, the difference is too small to distinguish.

Note that the energies are calculated for the Fermi level of -0.17 eV, for Fermi level of -0.19 eV, the calculated values are provided at the end of this summery.

In principle, the exciton 1s-2p transition energy can be estimated by performing the quasiparticle GW and Bethe-Salpeter equation (BSE) calculations. To model the experimental condition herein for the boron doped graphene/MoSe2 heterojunction, however, the system constructed should contain more than 1200 atoms (the supercell of graphene should larger than 26×26). On the other hand, to achieve well-converged quasiparticle energies, especially when there is transition metal element (Mo) in the system, a dense enough (21×21×1) k-gird, a large energy cutoff (~40Ry) and a large number (>10000) of unoccupied states is needed12, 25. The calculation cost is therefore far beyond computing resource we can afford.

Supplementary Note 12: Al-doped Graphene

598 To explore the possible effect of dopant rather than Fermi level on the binding
599 energy, we also compute the interlayer exciton binding energy with Al-doped
600 graphene.

601 As demonstrated in *Supplementary Figure 15*, the Fermi energy levels are
602 adjusted, by aluminum doping, to the valence bands and the whole doping system also
603 acts as a p-dopant. *Supplementary Figure 15* shows the Fermi energy levels of the
604 doped graphene with different N×N primitive cells. With the decrease of dopant
605 concentration, the Fermi energy level gradually decreases to the experimental value.
606 As the Fermi energy level of aluminum-doped graphene reaches the experimental
607 value (-0.17eV), the primitive cell size is 13×13 (Supplementary Figure 16), and the
608 calculated effective mass of Al-doped system for electron and hole is 0.0122 and
609 0.0135, respectively. (Supplementary Figure 17)

610 When the hole is in graphene and the electron is in the $MoSe_2$ layer, the effective
611 mass of exciton can be obtained from $1/(\mu) = 1/(m_h^*) + 1/(m_e^*)$, where the effective
612 mass of monolayer $MoSe_2$ conduction band $m_e^* = 0.502 m_0$ (Supplementary Figure 18)
613 and the effective mass of Al-doped graphene valence band $m_h^* = 0.0122 m_0$. m_0 is
614 the free electron mass. Based on the finite element method, we then solved the
615 Schrödinger equation on a 2×10^3 Å circle plane, with the effective mass of the
616 excitonic quasi particle and aforementioned Coulomb potential. The eigenvalues and
617 selected eigenfunctions calculated are presented in Supplementary Figure 18A. The
618 exciton transition energy between 1s and 2p is $E_{1s\text{-}2p}$= 0.275 eV, and the means radius
619 of wave functions for 1s CT is $\left\langle \rho_{CT_{1S}} \right\rangle = 45.7\text{Å}$.

When electron is in graphene and hole is in $MoSe_2$, the hole and electron effective masses should be the effective masses of the monolayer $MoSe_2$ valence band $0.583\,m_0$ and Al-doped graphene conduction band $0.0135\,m_0$, respectively. The eigenvalues and selected eigenfunctions are presented in Supplementary Figure 18b. The exciton transition energy between 1s and 2p is $E_{1s\text{-}2p}$= 0.292 eV, and the means radius of wave functions for 1s CT is $\left\langle \rho_{CT_{1S}} \right\rangle = 42.3\text{Å}$.

Supplementary Note 13: Both electron and hole effective masses of graphene are $0.012m_0$

Using $0.012m_0$ reported for a CVD-grown graphene (JAP, 113, 043708, 2013), we also calculate the interlayer binding energy.

In summary, the binding energy is only slightly affected by the nature of dopant. In three different calculations, the binding energy is between 0.265~0.292 eV. All are very close to the experimental value.

Supplementary Note 14: Origin of carrier reduced mass in graphene and large interlayer binding energy

It is well known that the effective mass of the pristine graphene is zero, i.e., the effect mass of the state at **k** = 0 (Dirac point, at which the Fermi level lie in the pristine graphene) is zero. However, when the **k** point deviates from the Dirac point, e.g., the Fermi level shifts due to the effect of doping, the effective mass is no longer zero. We can approximately evaluate this effect based on a tight-binding (TB) model.

642 Under a TB approach, the energy dispersion of graphene near the Fermi points is
643 expressed as Dirac cones:

644 $$E(\mathbf{k}) = \frac{3}{2} t_0 a_0 |\mathbf{k}|, \tag{22}$$

645 where a_0 = 2.42 Å is the equilibrium C-C bond length, and $t_0 \approx 2.7$ eV is the hopping
646 energy between the nearest C atoms. The effective mass at **k** is defined as

647 $$m^*(\mathbf{k}) = \frac{\hbar^2}{\frac{\partial^2 E(\mathbf{k})}{\partial \mathbf{k}^2}}. \tag{23}$$

648 When $\mathbf{k} \neq 0$, the energy dispersion along the normal direction has a finite curvature
649 (effective mass) as shown as the solid lines in Supplementary Figure 21. Based on
650 Supplementary Equation (22) and (23), the effective mass of electrons at the Fermi
651 level (chemical potential μ) along the normal direction is given as

652 $$m^*\Big|_{E(\mathbf{k})=\mu} = \frac{4\hbar^2}{9 t_0^2 a_0^2} |\mu|. \tag{24}$$

653 The dependence of the effective mass on the chemical potential is plotted in
654 Supplementary Figure 22. It can be seen that $m^* = 0$ for pristine graphene ($\mu = 0$), but
655 it linearly increases with increasing $|\mu|$. For $\mu = -0.17$ eV, $m^* \approx 0.039 m_0$. If we
656 roughly regard the effective mass along the radical direction as unchanged (equal to 0
657 as that in pristine graphene), a direct average on both the normal and radical
658 directions give $m^* \approx 0.02 m_0$ under $\mu = -0.17$ eV. This estimated value is actually very
659 close to $m^* \approx 0.0116 m_0$ from the ab initio calculations assuming B-doped.

660 In 3D systems, the electric potential of a point charge under the screening of a
661 dielectric surrounding with a relative dielectric constant ε is described by a screened
662 Coulomb potential (in atomic units)

$$V_{3D}(\mathbf{r}) = \frac{1}{\varepsilon r} \tag{25}$$

by solving the Poisson's equation, which gives the exciton binding energy of the hydrogen-like model:

$$E_{b,3D}(\mathbf{r}) = \frac{m^*}{2\varepsilon^2}, \tag{26}$$

where m^* is the reduced effective mass. Supplementary Equation (26) suggests that E_b is proportional to m^*.

However, for a 2D dielectric sheet embedded into vacuum such as single-layer $MoSe_2$ or other 2D systems considered in experiments, the 2D screened potential is not given as a screened Coulomb potential:

$$V_{2D}(\mathbf{r}) \neq \frac{1}{\varepsilon r}, \tag{27}$$

but is given as a complicated function in terms of the Struve function and the second kind Bessel function [refer to: P. Cudazzo, I. V. Tokatly, and A. Rubio, *Phys. Rev. B* **84**, 085406 (2011)], which was also listed as Supplementary Equation (19). As a result, the binding energy of 2D exciton is not described by Supplementary Equation (26), but is given as [refer to: T. Olsen, S. Latini, F. Rasmussen, and K. S. Thygesen, *Phys. Rev. Lett.* **116**, 056401 (2016)]

$$E_{b,2D} = \frac{8m^*}{\left(1+\sqrt{1+\frac{32\pi\alpha m^*}{3}}\right)^2}, \tag{28}$$

where α is the 2D polarizability calculated as $\alpha = L\frac{\varepsilon-1}{4\pi}$ where ε is the dielectric constant of bulks and L is the thickness of the 2D sheet. A remarkable property in Supplementary Equation (28) is that E_b is no longer linearly proportional to m^*. When

683 αm^* is large enough, we have $E_{b,2D} \approx \frac{3}{4\pi\alpha}$ which is independent on m^*.
684 Supplementary Equation 26 is applicable to both undoped and doped 2D systems. An
685 exciton is formed between an electron and a hole no matter whether the system is
686 doped or undoped, and the influence of doping just lies in its screening effect. As the
687 Fermi energy level of boron-doped graphene reaches the experimental value (−0.17
688 eV), the primitive cell size is 26.1 (refer to page 17 of SI), and the doping ratio is
689 actually small (less than 0.2%). Our ab initio calculation shows that the in-plane
690 dielectric constant of B-doped graphene is almost equal to the value of pristine
691 graphene when the primitive cell size is larger than 8 (refer to page 19 of SI).
692 Therefore, the screening effect in doped graphene is very weak.

693 Take the graphene-$MoSe_2$ as an example, $\bar{\varepsilon} \approx 4.97$ and L ≈ 10.4 Å, so we have α
694 = 6.17 (in atomic units). E_b is plotted in Supplementary Figure 23 as a function of m^*
695 based on Supplementary Equation (28), measured with respective to that of $m^* = 0.6$
696 (the value for $MoSe_2$). The result of Supplementary Equation (26) is also plotted to
697 provide a comparison. It can be seen that the dependence of E_b on m^* is higly
698 nonlinear for the 2D result in Supplementary Equation (28). For $m^* = 0.01m_0$, the 3D
699 result in Supplementary Equation (26) gives $E_b(m^* = 0.01)/E_b(m^* = 0.6) = 1/60$, i.e.,
700 the binding energy for $m^* = 0.01$ of graphene-$MoSe_2$ is 60 times smaller compared to
701 that of $MoSe_2$ as indicated by the reviewer, but the 2D result in Supplementary
702 Equation (28) gives $E_b(m^*=0.01)/E_b(m^*=0.6) \approx 1/3.1$. In other words, with the 2D
703 equation, the binding energy for $m^* = 0.01$ of graphene-$MoSe_2$ is merely 3.1 times
704 smaller compared to that of $MoSe_2$. Taking the 0.4-0.6 eV binding energy for the latter,

705 one may expect a binding enery of 0.13-0.19 eV for the graphene-$MoSe_2$ exciton,
706 which is close to the results from our measurements. In our work, we used a more
707 sophisticated theory that has been tested with other 2D systems (JACS 2015, 137,
708 8313-8320; Nat. Commun. 2016, 7, 12512) to calculate the binding energy and it
709 turns out to be very close to the experimental value. The dependence of calculated
710 1s-2p transition energy on reduced mass is plotted in Supplementary Figure 12.
711

Supplementary References

1. Dawlaty JM*, et al.* Measurement of the optical absorption spectra of epitaxial graphene from terahertz to visible. *Applied Physics Letters* **93**, (2008).

2. Gusynin VP, Sharapov SG, Carbotte JP. Unusual microwave response of Dirac quasiparticles in graphene. *Phys Rev Lett* **96**, (2006).

3. Mikhailov SA, Ziegler K. New electromagnetic mode in graphene. *Phys Rev Lett* **99**, (2007).

4. Malard LM, Mak KF, Neto AHC, Peres NMR, Heinz TF. Observation of intra- and inter-band transitions in the transient optical response of graphene. *New J Phys* **15**, (2013).

5. Ma Q*, et al.* Tuning ultrafast electron thermalization pathways in a van der Waals heterostructure. *Nature Physics* **12**, 455-+ (2016).

6. Kampfrath T, Perfetti L, Schapper F, Frischkorn C, Wolf M. Strongly coupled optical phonons in the ultrafast dynamics of the electronic energy and current relaxation in graphite. *Phys Rev Lett* **95**, (2005).

7. Piscanec S, Lazzeri M, Mauri F, Ferrari AC, Robertson J. Kohn anomalies and electron-phonon interactions in graphite. *Phys Rev Lett* **93**, (2004).

8. Li ZZ, Wang JY, Liu ZR. Intrinsic carrier mobility of Dirac cones: The limitations of deformation potential theory. *J Chem Phys* **141**, (2014).

9. Park CH*, et al.* Electron-Phonon Interactions and the Intrinsic Electrical Resistivity of Graphene. *Nano Lett* **14**, 1113-1119 (2014).

10. Lui CH, Mak KF, Shan J, Heinz TF. Ultrafast Photoluminescence from Graphene. *Phys Rev Lett* **105**, (2010).

11. Zhang WJ*, et al.* Ultrahigh-Gain Photodetectors Based on Atomically Thin Graphene-MoS2 Heterostructures. *Scientific Reports* **4**, (2014).

12. Ugeda MM*, et al.* Giant bandgap renormalization and excitonic effects in a monolayer transition metal dichalcogenide semiconductor. *Nat Mater* **13**, 1091-1095 (2014).

13. Berkelbach TC, Hybertsen MS, Reichman DR. Theory of neutral and charged excitons in monolayer transition metal dichalcogenides. *Phys Rev B* **88**, (2013).

14. Hong XP*, et al.* Ultrafast charge transfer in atomically thin MoS2/WS2 heterostructures. *Nat Nanotechnol* **9**, 682-686 (2014).

15. Chen HL*, et al.* Ultrafast formation of interlayer hot excitons in atomically thin MoS2/WS2 heterostructures. *Nat Commun* **7**, 12512 (2016).

16. Wang HN, Zhang CJ, Rana F. Ultrafast Dynamics of Defect-Assisted Electron Hole Recombination in Mono layer MoS2. *Nano Lett* **15**, 339-345 (2015).

17. Poellmann C*, et al.* Resonant internal quantum transitions and femtosecond radiative decay of excitons in monolayer WSe2. *Nat Mater* **14**, 889-+ (2015).

18. Kaindl RA, Hagele D, Carnahan MA, Chemla DS. Transient terahertz spectroscopy of excitons and unbound carriers in quasi-two-dimensional electron-hole gases. *Phys Rev B* **79**, (2009).

19. Kresse G, Furthmuller J. Efficient iterative schemes for ab initio total-energy calculations using a plane-wave basis set. *Phys Rev B* **54**, 11169-11186 (1996).

20. Perdew JP, Burke K, Ernzerhof M. Generalized gradient approximation made simple. *Phys Rev Lett* **77**, 3865-3868 (1996).

21. Monkhorst HJ, Pack JD. SPECIAL POINTS FOR BRILLOUIN-ZONE INTEGRATIONS. *Phys Rev B* **13**, 5188-5192 (1976).

22. Grimme S, Antony J, Ehrlich S, Krieg H. A consistent and accurate ab initio parametrization of density functional dispersion correction (DFT-D) for the 94 elements H-Pu. *J Chem Phys* **132**, (2010).

23. Ramasubramaniam A. Large excitonic effects in monolayers of molybdenum and tungsten dichalcogenides. *Phys Rev B* **86**, (2012).

24. Zhu XY, Monahan NR, Gong ZZ, Zhu HM, Williams KW, Nelson CA. Charge Transfer Excitons at van der Waals Interfaces. *J Am Chem Soc* **137**, 8313-8320 (2015).

25. Qiu DY, da Jornada FH, Louie SG. Optical Spectrum of MoS2: Many-Body Effects and Diversity of Exciton States. *Phys Rev Lett* **111**, (2013).

26. Tonndorf P*, et al.* Photoluminescence emission and Raman response of monolayer MoS2, MoSe2, and WSe2. *Opt Express* **21**, 4908-4916 (2013).